Diagram, valence-to-core, and hypersatellite K β X-ray transitions in metallic chromium

Faisal Zeeshan, Joanna Hoszowska, Jean-Claude Dousse, Dimosthenis Sokaras, Tsu-Chien Weng, Roberto Alonso-Mori, Matjaz Kavčič, Mauro Guerra, Jorge Miguel Sampaio, Fernando Parente, et al.

Received: 1 October 2018 | Revised: 17 January 2019 | Accepted: 18 January 2019

DOI: 10.1002/xrs.3019

SPECIAL ISSUE ARTICLE

WILEY

Diagram, valence-to-core, and hypersatellite $K\beta$ X-ray transitions in metallic chromium

Faisal Zeeshan[1] | Joanna Hoszowska[1] | Jean-Claude Dousse[1] | Dimosthenis Sokaras[2] | Tsu-Chien Weng[2] | Roberto Alonso-Mori[3] | Matjaz Kavčič[4] | Mauro Guerra[5] | Jorge Miguel Sampaio[6] | Fernando Parente[5,8] | Paul Indelicato[8] | José Pires Marques[7] | José Paulo Santos[5]

[1]Department of Physics, University of Fribourg, Fribourg, Switzerland

[2]Stanford Synchrotron Radiation Lightsource, SLAC National Accelerator Laboratory, Menlo Park, USA

[3]Linac Coherent National Accelerator Laboratory, SLAC National Accelerator Laboratory, Menlo Park, USA

[4]Jožef Stefan Institute, Department of Low and Medium Energy Physics, Ljubljana, Slovenia

[5]Laboratório de Instrumentação, Engenharia Biomédica e Física da Radiação (LIBPhys-UNL), Departamento de Física, Faculdade de Ciências e Tecnologia, FCT, Universidade Nova de Lisboa, Caparica, Portugal

[6]Space Radiation Environments, LIP-Laboratório de Instrumentação e Física Experimental de Partículas, Lisboa, Portugal

[7]BioISI-Biosystems and Integrative Sciences Institute, Faculdade de Ciências da Universidade de Lisboa, Lisboa, Portugal

[8]Laboratoire Kastler Brossel, Ecole Normale Supérieure, CNRS, Sorbonne Universités, UPMC Univ. Paris 06, Paris, France

Correspondence
Joanna Hoszowska, Department of Physics, University of Fribourg, Chemin du Musée 3, Fribourg CH-1700, Switzerland.
Email: joanna.hoszowska@unifr.ch

We report on measurements of the $K\beta$ diagram, valence-to-core (VtC), and hypersatellite X-ray spectra induced in metallic Cr by photon single and double K-shell ionization. The experiment was carried out at the Stanford Synchrotron Radiation Lightsource using the seven-crystal Johann-type hard X-ray spectrometer of the beamline 6-2. For the $K\beta$ diagram and VtC transitions, the present study confirms the line shape features observed in previous works, whereas the $K^h\beta$ hypersatellite transition was found to exhibit a complex spectral line shape and a characteristic low-energy shoulder. The energy shift of the hypersatellite relative to the parent diagram line was deduced from the measurements and compared with the result of extensive multiconfiguration Dirac–Fock (MCDF) calculations. A very good agreement between experiment and theory was found. The MCDF calculations were also used to compute the theoretical line shape of the hypersatellite. A satisfactory agreement was obtained between the overall shapes of the experimental and theoretical spectra, but deviations were observed on the low- and high-energy flanks of the hypersatellite line. The discrepancies were explained by chemical effects, which were not considered in the MCDF calculations performed for isolated atoms.

Funding information
Swiss National Science Foundation, Grant/Award Number: 2000020-146739; Faculdade de Ciências e Tecnologia, Universidade Nova de Lisboa, Grant/Award Number: PTDC/FIS-AQM/31969/2017 and SFRH/BPD/92455/2013; FCT/MCTES/PIDDAC, Grant/Award Number: UID/FIS/04559/2013 and UID/MULTI/04046/2013

1 | INTRODUCTION

X-ray emission spectroscopy of inner-core and valence-to-core (VtC) transitions in resonant and non-resonant excitation conditions is a powerful technique to probe the atomic structure of matter.[1–5] For 3*d* transition metals, *Kβ* X-ray emission spectroscopy spectra provide information on the electronic structure of the samples as well as on their oxidation state and spin state. The solid and chemical effects on the $K\beta_{1,3}$ diagram and the $K\beta_{2,5}$ VtC transitions are well known, and numerous measurements of the *Kβ* X-ray emission spectra of 3*d* transition metals and their chemical compounds have been performed using photons from X-ray tubes[6,7] and synchrotron radiation,[1,3,5,8] electrons,[9] and protons[10–12] for the targets excitation. In these experiments, the energy shifts, intensity ratios, relative positions, and widths of the *Kβ* transitions were investigated.

In contrast, high-energy resolution data for photoinduced $K^h\beta_{1,3}$ hypersatellite transitions are scarse (see Figure 4 in Section 5) because of the low-double-*K*-shell photoionization cross sections,[13–15] and transition yields (e.g., for Cr the intensity ratio of the $K^h\beta$ hypersatellite to the strongest diagram transition, *Kα* is only about 5×10^{-5}). Actually, only two high-resolution measurements of the $K^h\beta_{1,3}$ hypersatellite transitions induced by photon impact have been published so far, those of Diamant et al.[16] for elemental Fe and of Huotari et al.[17] for Ti metal.

High-energy resolution and high-collection efficiency are prerequisites in order to measure X-ray line energy shifts of few eV or less, as well as to evince small variations in X-ray line intensities and spectral shapes. Efficient collection of X-rays with high energy resolution can be achieved by using curved-crystal X-ray spectrometers. Various hard X-ray spectrometers based on Bragg reflections from single or multiple perfect crystals have been developed.[18–23] Nowadays, several synchrotron facilities offer hard X-ray beam lines, which are equipped with high resolution multicrystal spectrometers.[24–27]

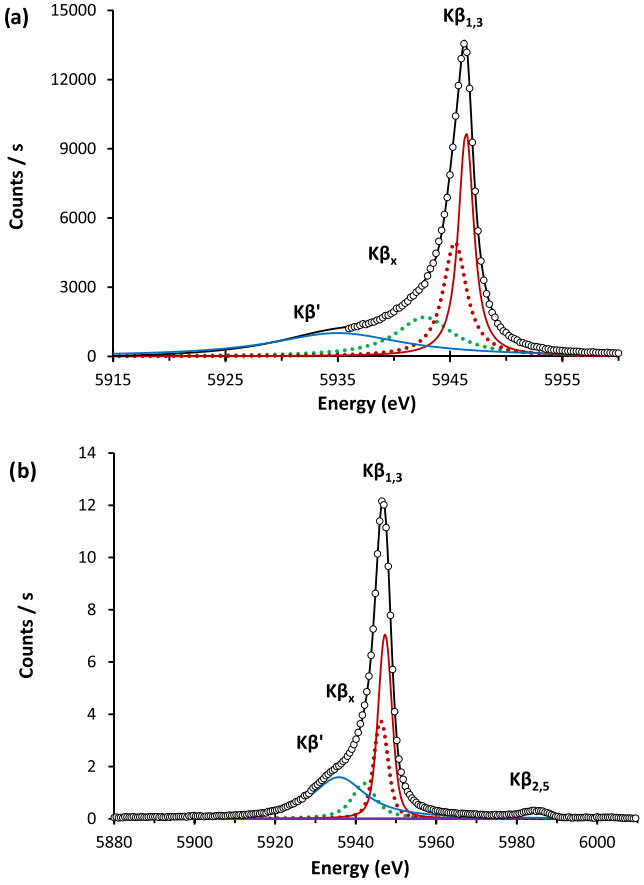

FIGURE 1 (a) Fit of the K$\beta_{1,3}$ spectrum of Cr measured at Stanford Synchrotron Radiation Lightsource (SSRL). Shown are the background subtracted experimental spectrum (open circles), the total fit (black curve) together with the four individual Voigt components of the fit: The red solid and red dotted lines for the main $K\beta_{1,3}$ transition, the green dotted line for the $K\beta_x$ transition, and the blue line for the $K\beta'$ transition. (b) Same as (a) but for the $K\beta_{1,3}$ spectrum measured in Fribourg. In the latter measurement, the energy range was extended to include the $K\beta_{2,5}$ transition

The $K^h\beta$ hypersatellite transitions result from the radiative decay of double *K*-shell vacancy states through the *M*-shell. The $K^h\beta_1$ $\left(1s^{-2} \rightarrow 1s^{-1}3p_{3/2}^{-1}\right)$ and $K^h\beta_3$ $(1s^{-2} \rightarrow 1s^{-1}3p_{1/2}^{-1})$ hypersatellite transitions are electric dipole

transitions. The $K^h\beta_3$ hypersatellite is allowed in both the LS and jj coupling schemes, while the $K^h\beta_1$ hypersatellite corresponds to the spin-flip $^1S_0 \rightarrow {}^3P_1$ transition, which is forbidden by the E1 selection rules in the LS coupling scheme. For low Z elements for which the LS coupling scheme prevails, the $K^h\beta_1$ transition is thus not observable, and the I($K^h\beta_1$)/I($K^h\beta_3$) yield ratio reflects the degree of intermediacy of the coupling.[28,29]

The objective of this work was to investigate the $K^h\beta_{1,3}$ hypersatellite spectrum of elemental Cr induced by single-photon double K-shell ionization. A particular aim was to compare the experimentally determined energy shift of the hypersatellite with respect to its parent diagram line and the hypersatellite line shape to theoretical predictions based on multiconfiguration Dirac–Fock (MCDF) calculations. Furthermore, in view of a future project aiming to compare the chemical sensitivity of the $K^h\beta$ hypersatellite transitions of 3d transition elements with the one of the VtC transitions, the $K\beta_{2,5}$ X-ray line of metallic Cr was also measured.

2 | EXPERIMENT

The experiment was performed at the Beamline 6–2 of the Stanford Synchrotron Radiation Lightsource (SSRL). The Beamline 6–2 is equipped with two liquid nitrogen cooled Si(111) and Si(311) crystal monochromators, and the incident X-ray beam is provided by a 0.9 T 56-pole wiggler. The high flux and monochromaticity of the photon beam and the wide solid angle of detection allow studying weak atomic processes even for relatively low-density samples. Rh-coated mirrors were positioned before and after the monochromators for focusing and collimation of the beam. A beam size of about 170-μm vertical and 400-μm horizontal was delivered at the sample position. The incident beam flux was typically 1-2×10^{13} photons/s. For the measurements of the Cr $K\beta$ spectra ($K\beta_{1,3}$ and $K\beta_{2,5}$ transitions), the photon beam energy was set to 6.1 keV, whereas for the $K^h\beta_{1,3}$ hypersatellite a beam energy of 13.7 keV close to the maximum of the double K-shell photoionization cross section for Cr was chosen.

For the measurements of the X-ray emission spectra, the seven-crystal Johann-type hard X-ray spectrometer[23] installed at the Beamline 6–2 was employed. The Johann geometry is semifocusing in which the crystal planes are bent to a radius 2R, where R is the radius of the Rowland circle but the crystal inner surface is not grounded. In order to reduce the geometrical effects,[30] the Rowland circle is placed on a vertical plane as the vertical beam size is smaller. The analyzer crystals are spherically bent to a radius of 1 m with a projected diameter of 100 mm. All crystal modules are placed on a common plate that can be moved vertically with the help of stepping motors. Each crystal module can move along its normal direction so that the crystals can follow the exact Rowland circle as the spectrometer is scanned. The spectrometer sustends a backscattering Bragg angular range of 88° to 74° .

In the present experiment, five Ge(440) analyzer crystals for the Cr $K\beta$ spectra and seven Si(333) crystals for the $K^h\beta_{1,3}$ transitions were employed. The Bragg angle for the Cr $K\beta_{1,3}$ was 85.9° and for the $K^h\beta_{1,3}$ lines 82.3° . The diffracted X-rays from all crystals were recorded simultaneously with a silicon drift detector detector placed on the vertical axis. The full width at half maximum (FWHM) energy resolution of the silicon drift detector was about 150 eV at 5.9 keV. As the spectrometer was operated at atmospheric pressure, a helium filled bag was placed between the crystal analyzers and the detector to minimize the attenuation and the diffuse scattering of X-rays. For each energy point, the incident photon beam intensity was monitored with ionization chambers. The photon beam energy was calibrated using the K-edge energies of Cr and Mn as references. The energy resolution and the energy calibration of the spectrometer were determined from the elastically scattered peaks in the photon energy domain of interest. For the Cr $K\beta$ transitions, the experimental resolution (FWHM) was 0.47 eV and for the $K^h\beta_{1,3}$ lines 0.49 eV. For the $K\beta_{1,3}$ diagram and $K\beta_{2,5}$ VtC transitions, the data were collected in two successive scans with an acquisition time of 1 s per point, whereas for the $K^h\beta_{1,3}$ hypersatellite transition six scans with a collection time of 5 s per point were performed.

3 | DATA ANALYSIS

The spectra were fitted by means of a least squares fitting program using the software package PeakFit®. Voigt functions were employed because they correspond to the convolution of the Gaussian and Lorentzian functions,[31] which represent the instrumental response of the spectrometer and the natural line shape of the transitions, respectively. Prior to fitting, each spectrum was normalized with the photon beam intensity and the total acquisition time.

3.1 | $K\beta$ diagram and VtC transitions

The electronic configuration of Cr in the ground state is [Ar] $3d^5 4s^1$, with five unpaired electrons in the 3d subshell. The $K\beta_{1,3}$ line is generated in the $3p \rightarrow 1s$ transition and is the strongest among the $K\beta$ X-ray lines. The unpaired electron in the $3p^{-1}$ state is strongly coupled with the unpaired electrons in the partially filled 3d subshell. Due to the 3p3d exchange interaction, two transitions are possible depending on the spin orientation of the unpaired electron in the $3p^{-1}$ state with respect to that of the 3d electrons.

According to the dipole selection rules, if the spins are parallel the $K\beta_{1,3}$, transition line will occur, and if the spins are antiparallel, then the $K\beta'$ satellite line of lower energy will originate. A shoulder on the low-energy side of the main $K\beta_{1,3}$ line arises when a 3*d* electron flips its spin and is denoted as $K\beta_x$.[32] The $K\beta_5$ transition is dipole forbidden in free atoms. In solids, the $K\beta_{2,5}$ line reflects the valence band and corresponds to transitions from the 3*d* or 4*p* state to the 1*s* state.[33]

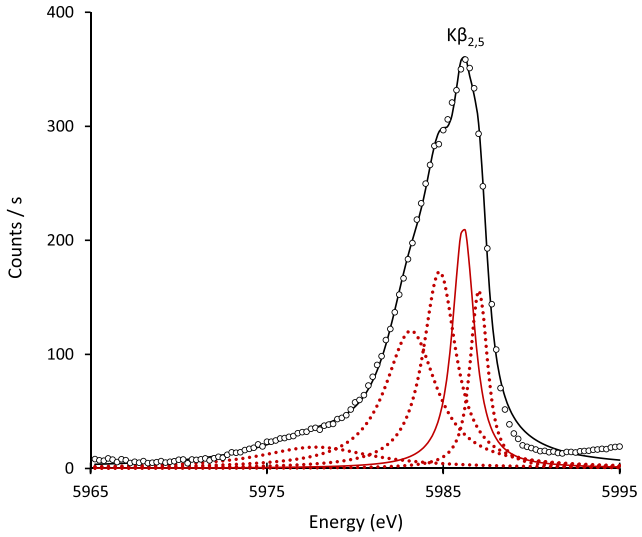

FIGURE 2 Fit of the $K\beta_{2,5}$ spectrum measured at Stanford Synchrotron Radiation Lightsource (SSRL). Shown are the measured spectrum (open circles) and the total fit (black curve). The red solid and dotted lines represent the individual Voigt components

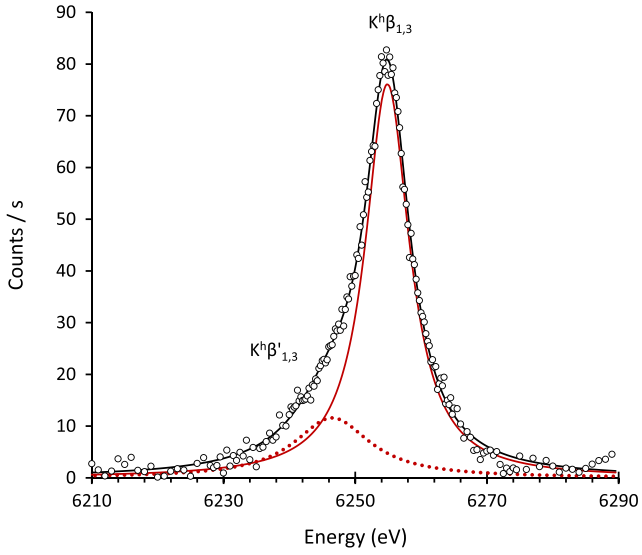

FIGURE 3 Fit of the $K^h\beta_{1,3}$ hypersatellite spectrum showing the measured spectrum (open circles) and the total fit (black curve). The fitted $K^h\beta_{1,3}$ component is depicted by the red solid line and the $K^h\beta'_{1,3}$ asymmetry by the red dotted line

In Figure 1a, we present the $K\beta_{1,3}$ X-ray emission spectrum of metallic Cr measured at SSRL. The spectrum was fitted with four Voigtians. Two Voigt functions were used for the $K\beta_{1,3}$ main component and one for the $K\beta_x$ and $K\beta'$ components, keeping the instrumental response function width fixed and all other parameters free. Since the limited angular range of the X-ray spectrometer does not allow for Bragg angles higher than 88°, the $K\beta'$ transition could not be measured with the Ge(440) crystal. For a reliable fit of the main $K\beta_{1,3}$ line, the $K\beta'$ transition should be, however, included. The fitting parameters for the $K\beta'$ transition were therefore determined from the Cr $K\beta_{1,3}$ spectrum collected in-house with the von Hamos spectrometer of Fribourg,[34] using an X-ray tube for the production of the target fluorescence. The fit of this spectrum is shown in Figure 1b. To obtain the values for the energy, width, and intensity of the $K\beta'$ line, the spectrum was analyzed using the fitting parameters reported by G. Hölzer et al.[6]

In Figure 2 shown is the fitted Cr VtC X-ray emission spectrum. The asymmetric $K\beta_{2,5}$ line was fitted with five Voigtians. The energies, intensities, and Lorentzian widths were free fitting parameters, whereas the instrumental width was kept fixed. The fitted linear background was subtracted beforehand in the presented X-ray spectrum.

3.2 | $K^h\beta$ Hypersatellite transition

In Figure 3, we present the $K^h\beta_{1,3}$ X-ray emission spectrum. The latter was fitted with two Voigtians, one corresponding to the highest peak assigned to the $K^h\beta_{1,3}$ hypersatellite transition and the second to the low energy asymmetry denoted as $K^h\beta'_{1,3}$. From the fit, an energy difference of 8.39(28) eV between the two components and a relative intensity $I(K^h\beta'_{1,3}/I(K^h\beta_{1,3})=0.27(1)$ were obtained. Only one Voigtian was used for the main line because the $K^h\beta_1$ and $K^h\beta_3$ hypersatellite transitions are highly overlapping due to the small expected separation ($\leq$ 2 eV)[28] and large lifetime widths,[16] and because the $K^h\beta_1$ to $K^h\beta_3$ intensity ratios reported by Chen et al.[29] and Costa et al.[28] are only 8% and 11%, respectively. The intensities, energies, and the Lorentzian widths of the Voigtians and the parameters of the linear background were used as free fitting parameters, whereas the instrumental response of the spectrometer was kept fixed in the fit.

4 | THEORY

Wave functions and binding energy values were calculated within the MCDF approach using the relativistic general purpose MCDF and general matrix elements code developed by Desclaux and Indelicato.[35,36] The electronic wave functions and energies are evaluated in the Coulomb field of the nucleus and the spherically averaged electronic field. The Breit interaction and the vacuum polarization terms

are also included in the self-consistent field calculation, and the self-energy is included as perturbation. A detailed description of the Hamiltonian and wave functions can be obtained in the previous studies.[37–41]

Having in view the calculation of the radiative decays, which were obtained using the relativistic expressions implemented in the MCDF general matrix elements code,[42–44] the so-called optimized levels (OL) method was followed to calculate the wave functions and energies of the levels involved in all possible transitions, using full relaxation of both initial and final states. Since the spin-orbitals of the initial and final levels were optimized separately, they are not orthogonal. To deal with the non-orthogonality of the wave functions, the code uses the formalism described by Löwdin.[45] The length gauge was used for all radiative transition probabilities.

Initial-state wave functions for the $K^h\beta$ hypersatellite transitions were generated for configurations that contain two initial inner-shell vacancies in the *K*-shell, whereas final state wave functions were generated for configurations that contain one vacancy in the *K*-shell and another one in an higher shell. Due to the very high number of levels and consequently of radiative transitions, multiconfiguration wave functions beyond intermediate coupling were not employed in the calculation.

For the simulation of the $K^h\beta$ hypersatellite spectrum, we have used the calculated transition rates, energies and the specific level degeneracy. Since the initial state for both the $K^h\beta_1$ and $K^h\beta_3$ lines is the same, and the final line intensity is normalized to the experimental spectrum, the fluorescence yield of the initial two-hole level is not needed for the simulation. Each of the 179,712 radiative transitions calculated in this work were turned into individual Voigtian distributions with a Gaussian width value equal to the spectrometer energy broadening, following a similar procedure as in the study of Guerra et al.[46]. The final synthesized spectrum is the sum of all the individual Voigtian components, without any fits to the experimental spectrum other than an energy offset due to the Auger shift, which was not calculated in this work.

5 | RESULTS AND DISCUSSION

5.1 | Energies and energy shifts

The energies of the Kβ hypersatellite and diagram transitions obtained in the present work are listed in Table 1. The energies of the $K^h\beta_{1,3}$ hypersatellite line and $K^h\beta'_{1,3}$ hypersatellite asymmetry component as well as the center of gravity energy of these two lines are listed. The peak energies of the $K\beta_{1,3}$ diagram and $K\beta_{2,5}$ VtC transitions (Voigtians represented by solid lines in Figures 1 and 2, respectively) as well as the center of gravity energies of the $K\beta_{1,3}$ and $K\beta_{2,5}$ transitions are also presented. For the center of gravity energy $\bar{E}(K\beta_{1,3})$, the $K\beta'$ component (see Figure 1) was not considered.

Present energy differences between the $K\beta_{2,5}$ VtC and $K\beta_{1,3}$ diagram transitions amount to 39.73(7) eV if one considers the peak energies and to 39.57(16) eV if one considers the center of gravity energies. Both results are consistent with the experimental values of 39.5(3) eV and 40.1(3) eV obtained with synchrotron radiation beams by Tirao et al.[47] and Deluigi et al.,[8] respectively, whereas the shift of 37.88 eV obtained by Iihara[48] with an X-ray tube and the one of 43.9(1.4) eV determined by Uršič et al.[10] with protons are significantly smaller, respectively, bigger, than the values found in this work.

The energy shift $\Delta E = E(K^h\beta_{1,3})$ - $\bar{E}(K\beta_{1,3})$ of the hypersatellite with respect to its parent diagram line is presented in Table 2 where it is compared with the theoretical shift obtained in the present work and to the one calculated by Costa et al.[28] If one assumes that the accuracy of the theoretical results is about 1 eV, our experimental value agrees with the theoretical one and with the prediction of Costa. To our best knowledge, no other experimental value is available in the literature for Cr, but there is an accurate value for Fe of 336.0(5) eV,[16] which is well in line with the theoretical prediction of Costa and three older and less precise values for Mn,[49] Ge, and In[50] of 345(35) eV, 390(20) eV, and 830(60) eV, respectively. The theoretical energy shifts calculated by Costa are plotted as a function of the atomic number *Z* in Figure 4 together with the experimental and theoretical results obtained in this work for Cr and the above mentioned other existing experimental data.

TABLE 1 Energies of the $K^h\beta_{1,3}$ hypersatellite and $K^h\beta'_{1,3}$ asymmetry component and the center of gravity energy $\bar{E}(K^h\beta_{1,3})$ of these two lines. The peak energies of the $K\beta_{1,3}$ and $K\beta_{2,5}$ transitions and the center of gravity energies $\bar{E}(K\beta_{1,3})$ and $\bar{E}(K\beta_{2,5})$ are also listed

$E(K^h\beta_{1,3})$	$E(K^h\beta'_{1,3})$	$\bar{E}(K^h\beta_{1,3})$	$E(K\beta_{1,3})$	$\bar{E}(K\beta_{1,3})$	$E(K\beta_{2,5})$	$\bar{E}(K\beta_{2,5})$
6254.88(3)	6246.49(28)	6253.14(6)	5946.42(2)	5945.09(3)	5986.15(7)	5984.66(16)

Note. All values are given in eV. The quoted uncertainties correspond to 1σ statistical errors from the fits.

5.2 | Spectral shapes and line widths

The measured spectral shapes of the $K\beta_{1,3}$ diagram line, and $K^h\beta_{1,3}$ hypersatellite are plotted in Figures 1 and 3. The plots clearly show that the spectral profiles of both transitions exhibit complex line shapes with characteristic low energy asymmetries. For the $K\beta$ diagram transition, the $3p3d$ exchange interaction, that depends on the number of unpaired $3d$ electrons, gives rise to predominantly low-spin ($K\beta_{1,3}$ main line), high-spin, ($K\beta'$) and spin-flip ($K\beta_x$) satellite transitions. In a simplified picture, the spin-orbit splitting and the $3p3d$ exchange interaction are the main factors determining the spectral shapes of the $K\beta_{1,3}$ diagram line. Regarding the $K^h\beta_{1,3}$ hypersatellite spectrum, the overall shape shows a spread in the multiplet structure over a larger energy as compared with the $K\beta_{1,3}$ diagram transition. The shorter lifetime of the initial double core-hole state results in a broadening of the spectral features and merging of components into each other. This is reflected in the bigger line width of the $K^h\beta_{1,3}$ hypersatellite transition.

The FWHM and the Lorentzian widths of the $K\beta_{1,3}$ main line and $K^h\beta_{1,3}$ hypersatellite obtained in this experiment

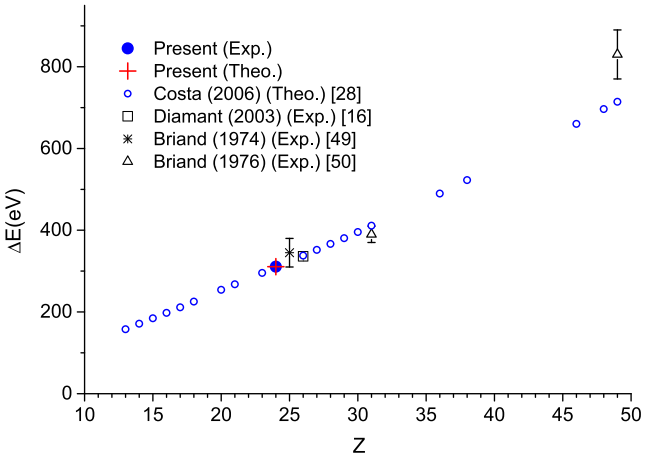

FIGURE 4 (color online) Energy shift ΔE of the $K^h\beta$ hypersatellite relative to the $K\beta$ diagram transition as a function of the atomic number Z. As shown, existing experimental data are scarce. Error bars of our result and the one of Diamant et al.[16] are to small to be seen

TABLE 2 Energy shift ΔE between the $K^h\beta_{1,3}$ hypersatellite and its $K\beta_{1,3}$ parent diagram line

Present (Exp.)	Present (Theo.)	Costa et al.[28]
309.79(4)	310.8	309.49[a]
310.85(6)		

Note. The second present value for the shift corresponds to the difference of the center of gravity energies of all spectral components of the hypersatellite and diagram spectra. Our experimental results are compared with theoretical predictions.

[a] Linear interpolation of the values quoted for V and Fe.

are presented in Table 3. For the $K\beta_{1,3}$ diagram transition, other existing experimental values are also presented. It is noteworthy that the $K^h\beta_{1,3}$ hypersatellite line width is larger than the value $\Gamma(K^h\beta_{1,3}) \cong 3 \cdot \Gamma_K + \Gamma_{M_{2,3}}$ expected from the sum of the initial state natural width $\Gamma_{KK} \cong 2 \cdot \Gamma_K$, where Γ_K stands for the $1s$ level width, and the natural width $\Gamma_K + \Gamma_{M_{2,3}}$ of the final states $1s^{-1}3p^{-1}_{1/2,3/2}$. Using for the atomic level widths the values recommended by Campbell and Papp,[51] the line width derived from the above formula yields a value of 4.3 eV, which is about a factor of two smaller than the measured line width. For the $K^h\alpha$ hypersatellite lines, in particular, in the case of $3d$ transition metals, such discrepancies have been already observed (see, e.g.,the studies of Hoszowska et al. and Diamant et al.[14,15]). From the reported $K^h\beta_{1,3}$ hypersatellite spectra plots for Sc,[52] Ti,[17] and Fe,[16] one can derive FWHM widths of about 7, 8, and 15 eV, respectively. The FWHM of Sc (Z=21) and Ti (Z=22) are comparable with the FWHM of 8.8 eV obtained in this work for Cr (Z=24), whereas the value found for Fe (Z=26) seems to be unexpectedly high as compared with those of the three lighter elements.

In Figure 5b one can see the comparison of the simulated and experimental spectrum. The agreement is satisfactory but the structures on the low-energy flank are not observed in the experimental spectrum, and the asymmetry on the high energy side of the measured spectrum is not reproduced by the calculations. The FWHM of the synthetized hypersatellite line amounts to 11.2 eV, whereas the measured FWHM is 8.8 eV. The main reason for the discrepancies is, very likely, that the calculations were performed for isolated atoms while the experiment was carried out with a bulk metallic sample. As pointed out before, the chemical environment of the target atoms in the experimental sample cannot be neglected, specially for atoms whose electronic structures are as complex as Cr, with a $3d$ half-filled shell. The molecular bonds of the bulk sample can significantly change the line shape due to changes made to selection rules for radiative transitions, as well as the change in orbital energies, which alone can enable new Auger channels which might be closed in isolated

TABLE 3 The full widths at half maximum (FWHM) and the natural line widths of the $K\beta_{1,3}$ main diagram line and $K^h\beta_{1,3}$ hypersatellite

	FWHM		Line width	
Line	Present	Other (Exp.)	Present	Other (Exp.)
$K\beta_{1,3}$	2.7	2.53[6]	1.47(7)	1.78(8)[8]
		2.68(5)[55]		1.80[55]
$K^h\beta_{1,3}$	8.8	-	8.14(6)	-
$K^h\beta'_{1,3}$	-	-	14.0(5)	-

Note. For the diagram line, present results, and available experimental data from the literature are given. All widths are quoted in eV.

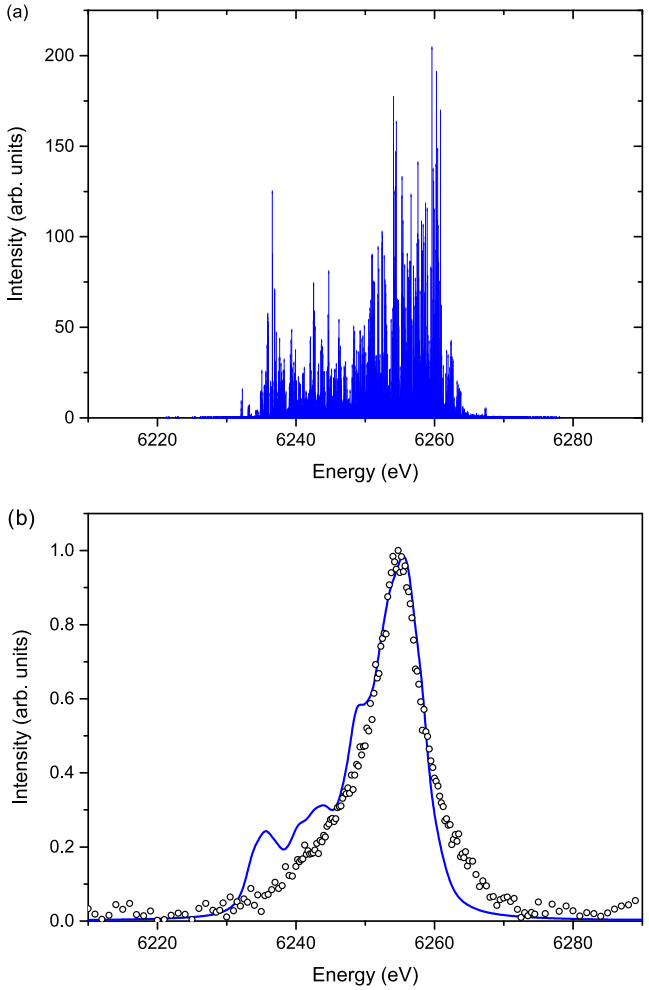

FIGURE 5 (a) Theoretical stick spectrum of the $K^h\beta_{1,3}$ transition. The positions of the sticks correspond to the energies of the different hypersatellite components and their heights to the transition probabilities of the latter. (b) Comparison between the simulated $K^h\beta_{1,3}$ hypersatellite spectrum (blue solid line) with the experimental one (open circles). The theoretical spectrum was obtained by summing all Voigtians attached to the components of the stick spectrum

atoms.[53,54] The calculated spin-orbit splitting appears to be narrower than in the experimental spectrum, as can be seen by the high energy tail, which is missing in the theoretical simulation. Nevertheless, the very good double Voigt fit of the experimental spectrum leads us to conclude that in fact, the chemical environment of the solid sample contributes to the narrowing of the spin-orbit splitting, which makes the $K^h\beta_1$ and $K^h\beta_3$ lines more symmetric.

6 | SUMMARY AND CONCLUDING REMARKS

In this work, we have investigated the energy, shape and line width of the $K^h\beta_{1,3}$ hypersatellite X-ray line of metallic Cr. For comparison, the $K\beta_{1,3}$ diagram line and the $K\beta_{2,5}$ VtC lines were also measured. The experiment was carried out at the SSRL using the seven-crystal Johann-type hard X-ray spectrometer. The high-energy resolution and high-collection efficiency of the X-ray spectrometer combined with a photon beam intensity of about 10^{13} photons/s allowed to measure the weak $K^h\beta_{1,3}$ hypersatellite with high precision. To the best of our knowledge, the $K^h\beta_{1,3}$ hypersatellite transition of Cr was measured for the first time.

The energies, energy shifts, line shapes, and line widths obtained in this work for the $K\beta_{1,3}$ diagram line and $K\beta_{2,5}$ VtC transitions were found to be in good agreement with the experimental and theoretical data available in the literature. For the $K^h\beta_{1,3}$ hypersatellite transition the obtained energy shift of 310.85(7) eV between the centroids of the hypersatellite and the $K\beta_{1,3}$ diagram transitions is in excellent agreement with the value of 310.8 eV predicted by the present MCDF calculations and also consistent with the value of 309.49 eV calculated earlier by Costa. For the FWHM of the $K^h\beta_{1,3}$ hypersatellite, a result of 8.8 eV was found, while the Lorentzian width of the main hypersatellite component deduced from the fit amounts to 8.14(6) eV, a result which is about a factor of two larger than the value expected from the sum of the widths of the initial and final states. The measured $K^h\beta_{1,3}$ hypersatellite spectrum was found to exhibit a complex spectral line shape with a spread in the multiplet structure over a larger energy range compared with the diagram transition. Two components, a main peak and a low energy shoulder, are characteristic of the $K^h\beta_{1,3}$ hypersatellite spectral shape. The latter was also determined from extensive MCDF calculations. A satisfactory agreement is obtained between the overall shapes of the experimental and theoretical spectra, but deviations are observed on the low- and high-energy flanks of the hypersatellite line. The discrepancies were explained by chemical effects which were not considered in the MCDF calculations.

ACKNOWLEDGEMENTS

The financial support of the Swiss National Science Foundation (Grant No. 200020-146739) is acknowledged by F. Z., J. H., and J.-Cl. D. M. G. acknowledges the support of the FCT, under the Contract No. SFRH/BPD/92455/2013 and the project PTDC/FIS-AQM/31969/2017, "Ultra-high-accuracy X-ray spectroscopy of transition metal oxides and rare earths." This work was also partly supported by the research center grants nos. UID/FIS/04559/2013 to LIBPhys-UNL, and UID/MULTI/04046/2013 to BioISI, from the FCT/MCTES/PIDDAC. Parts of this work have been carried out in the framework of the SPARC collaboration. We

are also thankful to the Standford Synchrotron Radiation Lightsource, which is a National User Facility operated by Standford University on behalf of the U.S. Department of Energy, Office of Basic Energy Sciences.

ORCID

Joanna Hoszowska https://orcid.org/0000-0003-4075-343X
José Pires Marques https://orcid.org/0000-0002-3797-3880

REFERENCES

[1] P. Glatzel, U. Bergmann, *Coord. Chem. Rev.* **2005**, *249*, 65.
[2] G Vankó, T. Neisius, G. Molnár, F. Renz, S. Kárpáti, A. Shukla, F. de Groot, *J. Phys. Chem. B* **2006**, *110*, 11647.
[3] V. A. Safonov, L. N. Vykhodtseva, Y. M. Polukarov, O. V. Safonova, G. Smolentsev, M. Sikora, S. G. Eeckhout, P. Glatzel, *J. Phys. Chem. B* **2006**, *110*, 23192.
[4] G. Smolentsev, A. V. Soldatov, J. Messinger, K. Merz, T. Weyhermüller, U. Bergmann, Y. Pushkar, J. Yano, V. K. Yachandra, P. Glatzel, *J. Am. Chem. Soc.* **2009**, *131*, 13161.
[5] N. Lee, T. Petrenko, U. Bergmann, F. Neese, S. DeBeer, *J. Am. Chem. Soc.* **2010**, *132*(28), 9715.
[6] G. Hölzer, M. Fritsch, M. Deutsch, J. Härtwig, E. Förster, *Phys. Rev. A* **1997**, *56*, 4554.
[7] K. Tsutsumi, H. Nakamori, K. Ichikawa, *Phys. Rev. B* **1976**, *13*, 929.
[8] M. T. Deluigi, G. Tirao, G. Stutz, C. Cusatis, J. Riveros, *Chem. Phys.* **2006**, *325*, 477.
[9] S. P. Limandri, A. C. Carreras, R. D. Bonetto, J. C. Trincavelli, *Phys. Rev. A* **2010**, *81*, 012504.
[10] M. Uršič, M. Kavčič, M. Budnar, *Nucl. Instr. and Meth. B* **2003**, *211*, 7.
[11] S. Fazinić, M. Jakšić, L. Mandić, J. Dobrinić, *Phys. Rev. A* **2006**, *74*, 062501.
[12] S. Fazinić, L. Mandić, M. Kavčič, I. Božičević, *Spectrochim. Acta Part B* **2011**, *66*, 461.
[13] J. Hoszowska, A. K. Kheifets, J.-Cl. Dousse, M. Berset, I. Bray, W. Cao, K. Fennane, Y. Kayser, M. Kavčič, J. Szlachetko, M. Szlachetko, *Phys. Rev. Lett.* **2009**, *102*, 073006.
[14] J. Hoszowska, J.-Cl. Dousse, W. Cao, K. Fennane, Y. Kayser, M. Szlachetko, J. Szlachetko, M. Kavčič, *Phys. Rev. A* **2010**, *82*, 063408.
[15] R. Diamant, S. Huotari, K. Hämäläinen, R. Sharon, C. C. Kao, M. Deutsch, *Phys. Rev. A* **2009**, *79*, 062511.
[16] R. Diamant, S. Huotari, K. Hämäläinen, R. Sharon, C. C. Kao, M. Deutsch, *Phys. Rev. Lett.* **2003**, *91*, 193001.
[17] S. Huotari, K. Hämäläinen, R. Diamant, R. Sharon, C.-C. Kao, M. Deutsch, *J. Electron Spectrosc. Relat. Phenom.* **2004**, *137*, 293.
[18] R. Alonso-Mori, J. Kern, R. J. Gildea, D. Sokaras, T.-C. Weng, B. Lassalle-Kaiser, R. Tran, J. Hattne, H. Laksmono, J. Hellmich, C. Glöckner, N. Echols, R. G. Sierra, D. W. Schafer, J. Sellberg, C. Kenney, R. Herbst, J. Pines, P. Hart, S. Herrmann, R. W. Grosse-Kunstleve, M. J. Latimer, A. R. Fry, M. M. Messerschmidt, A. Miahnahri, M. M. Seibert, P. H. Zwart, W. E. White, P. D. Adams, M. J. Bogan, S. Boutet, G. J. Williams, A. Zouni, J. Messinger, P. Glatzel, N. K. Sauter, V. K. Yachandra, J. Yano, U. Bergmann, *Proc. Natl. Acad. Sci. U.S.A.* **2012**, *109*, 19103.
[19] M. Kavčič, M. Budnar, A. Mühleisen, F. Gasser, M. Žitnik, K. Bučar, R. Bohinc, *Rev. Sci. Instrum.* **2012**, *83*, 033113.
[20] J. Hoszowska, J.-Cl. Dousse, *J. Electron Spectrosc. Relat. Phenom.* **2004**, *137-140*, 687.
[21] J. Szlachetko, M. Nachtegaal, E. de Boni, M. Willimann, O. Safonova, J. Sa, G. Smolentsev, M. Szlachetko, J. A. van Bokhoven, J.-Cl. Dousse, J. Hoszowska, Y. Kayser, P. Jagodzinski, A. Bergamaschi, B. Schmitt, C. David, A. Lücke, *Rev. Sci. Instrum.* **2012**, *83*, 103105.
[22] E. Kleymenov, J. A. van Bokhoven, C. David, P. Glatzel, M. Janousch, R. A. Mori, M. Studer, M. Willimann, A. Bergamaschi, B. Henrich, M. Nachtegaal, *Rev. Sci. Instrum.* **2011**, *82*, 065107.
[23] D. Sokaras, T.-C. Weng, D. Nordlund, R. A. Mori, P. Velikov, D. Wenger, A. Garachtchenko, M. George, V. Borzenets, B. Johnson, T. Rabedeau, U. Bergmann, *Rev. Sci. Instrum.* **2013**, *84*, 053102.
[24] H. Hayashi, M. Kawata, R. Takeda, Y. Udagawa, Y. Watanabe, T. Takano, S. Nanao, N. Kawamurac, *J. Electron Spectrosc. Relat. Phenom.* **2004**, *136*(1-2), 191.
[25] B. Dickinson, G. T. Seidler, Z. W. Webb, J. A. Bradley, K. P. Nagle, S. M. Heald, R. A. Gordon, I. M. Chou, *Rev. Sci. Instrum.* **2008**, *79*, 123112.
[26] J.-L. Hazemann, O. Proux, V. Nassif, H. Palancher, E. Lahera, C. Da Silva, A. Braillard, D. Testemale, M.-A. Diot, I. Alliot, W. Del Net, A. Manceau, F. Gélébart, M. Morand, Q. Dermigny, A. Shukla, *J. Synchrotron Rad.* **2009**, *16*, 283.
[27] L. Journel, L. E. Khoury, T. Marin, R. Guillemin, S. Carniato, A. Avila, R. Delaunay, C. F. Hague, M. Simon, *Rev. Sci. Instrum.* **2009**, *80*, 093105.
[28] A. M. Costa, M. C. Martins, J. P. Santos, F. Parente, P. Indelicato, *J. Phys. B: At. Mol. Opt. Phys.* **2006**, *39*, 2355.
[29] M. H. Chen, B. Crasemann, H. Mark, *Phys. Rev. A* **1982**, *25*, 391.
[30] U. Bergmann, S. P. Cramer, *Proc. SPIE* **1998**, *3448*, 198.
[31] G. K. Wertheim, M. A. Butler, K. W. West, D. N. E. Buchanan, *Rev. Sci. Instrum.* **1974**, *45*, 11.
[32] G. Peng, F. M. F. deGroot, K. Haemaelaeinen, J. A. Moore, X. Wang, M. M. Grush, J. B. Hastings, D. P. Siddons, W. H. Armstrong, O. C. Mullins, S. P. Cramer, *J. Am. Chem. Soc.* **1994**, *116*, 2914.
[33] U. Bergmann, C. R. Horne, T. J. Collins, J. M. Workman, S. P. Cramer, *Chem. Phys. Lett.* **1999**, *302*(1-2), 119.
[34] J. Hoszowska, J.-Cl. Dousse, J. Kern, C. Rhêmem, *Nucl. Instr. and Methods Phys. Res. A* **1996**, *376*, 129.
[35] J. P. Desclaux, *Comput. Phys. Commun.* **1975**, *9*, 31.
[36] P. Indelicato, J. Desclaux, MCDFGME, a multiconfiguration Dirac Fock and general matrix elements program, 2007 ; URL http.//dirac.spectro.jussieu.fr/mcdf.
[37] P. Indelicato, J. P. Desclaux, *Phys. Rev. A* **1990**, *42*, 5139.
[38] P. Indelicato, *Phys. Rev. A* **1995**, *51*, 1132.
[39] P. Indelicato, *Phys. Rev. Lett.* **1996**, *77*, 3323.
[40] J. P. Santos, G. C. Rodrigues, J. P. Marques, F. Parente, J. P. Desclaux, P. Indelicato, *Eur. Phys. J. D* **2006**, *37*, 201.
[41] M. C. Martins, A. M. Costa, J. P. Santos, F. Parente, P. Indelicato, *J. Phys. B: At. Mol. Phys.* **2004**, *37*, 3785.
[42] P. Indelicato, O. Gorveix, J. P. Desclaux, *J. Phys. B* **1987**, *20*, 651.
[43] O. Gorceix, P. Indelicato, J. P. Desclaux, *J. Phys. B* **1987**, *20*, 639.
[44] P. Indelicato, *Nucl. Instr. Methods Phys. Res. A* **1988**, *31*, 14.
[45] P.-O. Löwdin, *Phys. Rev.* **1955**, *97*, 1474.

[46] M. Guerra, J. M. Sampaio, T. I. Madeira, F. Parente, P. Indelicato, J. P. Marques, J. P. Santos, J. Hoszowska, J.-Cl. Dousse, L. Loperetti, F. Zeeshan, M. Müller, R. Unterumsberger, B. Beckhoff, *Phys. Rev. A* **2015**, *92*, 022507.

[47] G. Tirao, S. Ceppi, A. L. Cappelletti, E. P. Miner, *J. Phys. Chem. Solids* **2010**, *71*, 199.

[48] J. Iihara, T. Omori, K. Yoshihara, K. Ishii, *Nucl. Instrum. Methods B* **1993**, *75*, 32.

[49] J. P. Briand, P. Chevalier, A. Johmson, J. P. Rozet, M. Tavernier, A. Touati, *Phys. Lett. A* **1974**, *49*, 51.

[50] J. P. Briand, A. Touati, M. Frilley, P. Chevallier, A. Johnson, J. P. Rozet, M. Tavernier, S. Shafroth, M. O. Krause, *J. Phys. B* **1976**, *9*, 1055.

[51] J. L. Campbell, T. Papp, *At. Data Nucl. Data Tables* **2001**, *77*, 1.

[52] F. Zeeshan, J.-Cl. Dousse, J. Hoszowska, *J. Electron Spectrosc. Relat. Phenom* **2019**, (in press).

[53] M. Guerra, J. M. Sampaio, F. Parente, P. Indelicato, P. Hönicke, M. Müller, B. Beckhoff, J. P. Marques, J. P. Santos, *Phys. Rev. A* **2018**, *97*, 042501.

[54] Y. Ito, T. Tochio, M. Yamashita, S. Fukushima, A. M. Vlaicu, L. Syrocki, K. Slabkowska, E. Weder, M. Polasik, K. Sawicka, P. Indelicato, J. P. Marques, J. M. Sampaio, M. Guerra, J. P. Santos, F. Parente, *Phys. Rev. A* **2018**, *97*, 052505.

[55] H. Sorum, O. Weng, J. Bremer, *Phys. Status Solidi B* **1982**, *109*, 335.

How to cite this article: Zeeshan F, Hoszowska J, Dousse J-C, et al. Diagram, valence-to-core and hypersatellite Kβ X-ray transitions in metallic chromium. *X-Ray Spectrometry*. 2019;48:351–359. https://doi.org/10.1002/xrs.3019